Modeling of Laser Keyhole Welding: Part II. Simulation of Keyhole Evolution, Velocity, Temperature Profile, and Experimental Verification

HYUNGSON KI, PRAVANSU S. MOHANTY, and JYOTI MAZUMDER

This article presents the simulation results of a three-dimensional mathematical model using the level set method for laser-keyhole welding. The details of the model are presented in Part I.[4] The effects of keyhole formation on the liquid melt pool and, in turn, on the weld bead are investigated in detail. The influence of process parameters, such as laser power and scanning speed is analyzed. This simulation shows very interesting features in the weld pool, such as intrinsic instability of keyholes, role of recoil pressure, and effect of beam scanning.

For verification purposes, visualization experiments have been performed to measure melt-pool geometry and surface velocity. The theoretical predictions show a reasonable agreement with the experimental observations.

I. INTRODUCTION

IN the Part I of this work,[4] the authors have presented the model derivation for laser-keyhole welding, which considers three-dimensional fluid flow and heat transfer together with evolution of the liquid/vapor (L/V) and solid/liquid (S/L) interfaces. The numerical solution scheme adopted for this complex problem is also discussed in Part I. This article will present and discuss simulation results using practical welding parameters and interesting findings.

This article also presents experimental comparison of the model. Due to such intrinsic difficulties as high temperature, high melt-flow velocity, and extremely bright plasmas, experimental studies and measurements on the keyhole welding process are very limited. Matsunawa and co-workers visualized keyhole movements and flow patterns and measured approximate melt velocities inside the melt pool using the high-speed X-ray transmission imaging method.[6,2] They observed the weld-pool configuration by burying Sn/Pt wire along the weld line. They also observed the liquid flow in weld pool by preplacing fine tungsten particles of 100 to 400 μm in diameter between the two thin plates and analyzed the trajectories of W particles. However, it is still necessary to have velocity information on the melt surface, since the flow field is driven by surface phenomena, such as thermocapillary force and recoil pressure.

In this study, an optical visualization method[11] has been used to measure the weld-pool geometry. The images captured by a high-speed charge coupled device (CCD) camera are accurately calibrated and processed by image analysis software. In addition to the melt-pool geometry, the flow field predicted by the model needs to be verified. To the best of the author's knowledge, no experimental data are available regarding the melt-flow velocity on the surface. In this study, a method of estimating the melt-flow velocity on the L/V interface is suggested. Instead of directly measuring the melt-flow velocity, an attempt is made to trace the motion of a hump (or a disturbance), which is created by the keyhole fluctuation and convected on a current. Such a hump is believed to have wave characteristics. Thus, it propagates outward from the keyhole region at the phase velocity. This study claims that the movement of the hump center point can represent the flow velocity at that point. Experimental observations and measurements are compared with the model predictions.

HYUNGSON KI, Research Fellow, and JYOTI MAZUMDER, Professor, are with the Center for Laser Aided Intelligent Manufacturing, Mechanical Engineering Department, University of Michigan, Ann Arbor, MI 48109-2125. Contact e-mail: mazumder@engin.umich.edu PRAVANSU S. MOHANTY, Assistant Professor, is with the Mechanical Engineering Department, University of Michigan-Dearborn, Dearborn, MI 48126-1409.
Manuscript submitted November 8, 2001.

II. SIMULATION RESULTS

The parameters for the simulations are chosen based on the capability of our experimental facility to compare the results with the measurements. As an energy source, a continuous-wave CO_2 Gaussian laser beam with a 500-μm beam diameter is considered, and three laser powers, 2.4, 3.2, and 4 kW, are considered. Beam profile is assumed constant along the z direction. To understand the effect of beam scanning speed, three scanning speeds of 60, 80, and 100 ipm are selected. For the target material, steel sheets with a thickness of 1.214 mm are selected. Material properties are provided in Part I of this article.[4] In order to simulate a CO_2 laser beam, a laser-beam absorptivity of 0.1 is used for steel. The CO_2 laser, due to its relatively long wavelength of 10.6 μm, shows a poor laser-beam absorptivity.[10] It should be noted that the effective absorptivity changes as the keyhole evolves.

The simulation results for each case are similar in many respects, therefore, one case is discussed in detail, and the effects of scanning speed and laser power on the process will be studied in Section IV. The highest laser power with the lowest scanning speed ($P = 4$ kW and $V_s = 60$ ipm) is selected for an in-depth investigation. Simulation results for weld-pool shape, effective laser absorptivity, laser-intensity distribution, temperature field, pressure field, velocity field, and speed of forming a keyhole will be presented in the following sections. Effects of laser power and scanning

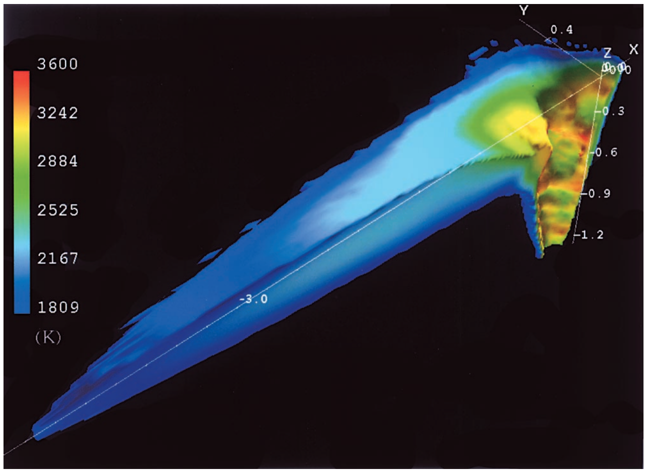

Fig. 1—Melt-pool shape with full penetration. Temperature distribution is shown on the liquid phase. (Laser power: 4 kW, scanning speed: 60 ipm, beam diameter: 500 μm, and 1.760 ms is elapsed after the process of forming a keyhole begins.)

speed will be presented together with experimental observations.

A. *Weld Pool Shape*

The shape of the weld pool after full penetration is presented in Figure 1. The temperature field is shown only on the liquid phase to visualize the melt area clearly. The S/L interface is marked by the constant melting temperature, *i.e.*, for steel, it is 1809 K. However, the actual melt pool predicted by the model is slightly larger than the one shown in Figure 1, since the mushy zone is not included in this figure. The mushy-zone size varies along the rear side of the melt-pool boundary.

The predicted melt-pool shape with a keyhole is realistic, compared to the experimental observation (Figure 1(B) in Reference 4). As expected, the length-to-width ratio of the weld pool is very large. For the weld pool shown in Figure 1, it is around 4.42 (length = 5.75 mm and width = 1.3 mm). This shows that the ability to transfer energy by fluid motion is superior in keyhole-mode welding, since the flow is highly pressurized due to recoil pressure. Therefore, it is essential to take the recoil pressure effect into account in the modeling of laser-keyhole welding.

It is also apparent from the figure that the rear part of the melt pool is swollen, which is caused by the highly pressurized liquid around the keyhole area. This result is in line with experimental observations.

Although many studies on keyhole phenomena are available in the literature, to the best of the authors' knowledge, this is the first complete prediction of the entire weld pool with a self-consistent keyhole profile.

B. *Effective Laser Absorptivity*

Figure 2(1) presents the effective laser absorptivity variation with time, and Figure 2(2) is the average number of ray reflections. Both plots are very similar in shape, as expected.

The two points marked in the figures by letters, A and B, denote the times when full penetration is about to occur at the bottom surface. After the first full penetration (point

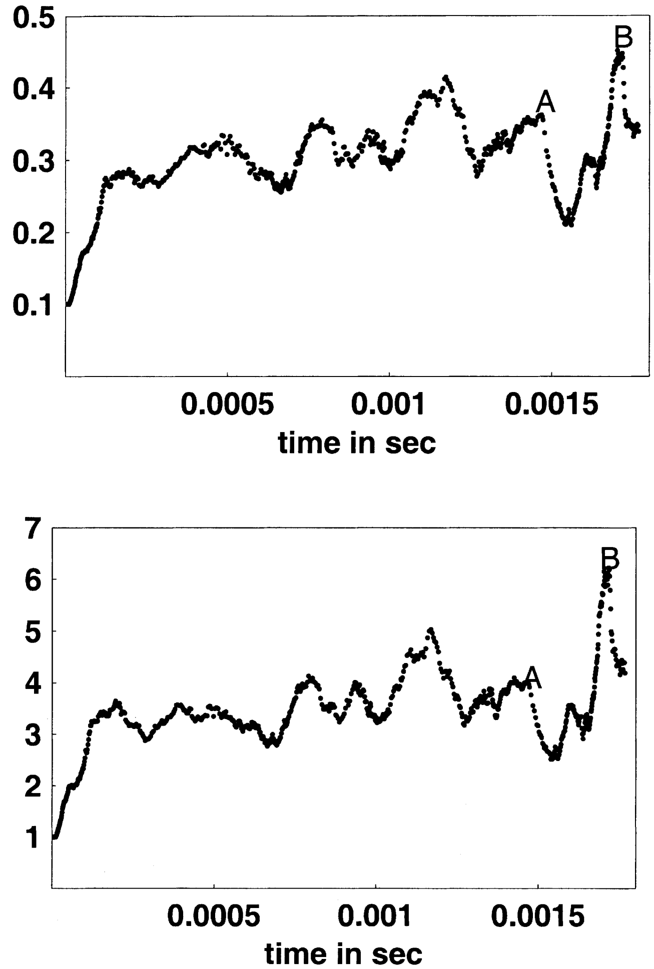

Fig. 2—(1) Top: effective laser beam absorptivity variation with time. (2) Bottom: average number of reflections against time (laser power: 4 kW, scanning speed: 60 ipm, and beam diameter: 500 μm).

A), the effective absorptivity drops considerably, and suddenly, the bottom hole is filled with liquid melt due to the decreased recoil pressure. At this point, the effective absorptivity increases again and then goes down with second penetration (point B).

It is clear that the effective laser absorptivity increases as the free surface deepens. The used laser-beam energy increases from 10 pct to around 45 pct (at point B), and the corresponding number of ray reflections rises to around 6.22 from the initial value, 1 (just one reflection per ray).

It is also obvious that effective absorptivity keeps fluctuating while increasing to the maximum value. This phenomenon can be associated with strong keyhole fluctuations and beam scanning effect. Therefore, intensity fluctuation drives keyhole fluctuation, and keyhole fluctuation, in turn, affects intensity fluctuation. This observation implies that keyhole fluctuation is an intrinsic phenomenon that exists at all times, no matter what process parameters are used. This result is supported by an experimental observation[6] that a keyhole is not stable but fluctuates violently even under constant laser powers.

After penetration, effective laser absorptivity decreases as part of the laser energy is lost through the bottom hole.

C. *Laser-Intensity Distribution*

Figure 3 presents the laser-intensity distribution variation with keyhole depth. Figure 3(1) is the Gaussian distribution for a flat surface at the reference time, which is defined as the time when the keyhole starts to form and is set to zero. The highest intensity point is located at the coordinate origin. As the keyhole deepens, however, this intensity profile is distorted in a very complicated manner.

Figure 3(2) is the laser-intensity profile redistributed in a shallow keyhole. The shallow keyhole wall, as expected, does not transform the beam profile much. As seen, it is nearly symmetric. Even in this case, however, the intensity profile is shifted a little bit to the tail side of the weld pool due to the scanning effect of the laser beam. As a result, the keyhole shape viewed from above ($+z$ direction) is circular with the maximum intensity point shifted a bit to the left ($-x$ direction). In short, scanning of the laser beam moves the intensity profile, and the laser-beam center is not coincident with the coordinate origin any more. In addition, the incoming laser beam now impinges on the front keyhole wall.

This characteristic becomes more noticeable as the keyhole deepens. Figures 3(3) through (8) show the dramatic evolution of the laser-intensity profile for deeper keyholes. Combined with the strong keyhole fluctuation, the redistributed intensity patterns are much more dynamic. As shown, in general, more than two local maxima exist in the redistributed laser intensity on the keyhole wall, and those maximum locations move/disappear and/or new maximum locations are created as the keyhole-wall fluctuates.

Figures 3(7) and (8) show the laser-intensity fields after the keyhole fully penetrates the target material. During the entire process, it is observed that the maximum laser intensity is only around 5 times higher than the original beam intensity. This reveals that the fluctuation and irregularity of the keyhole and the scanning of the laser beam more evenly distribute the beam energy on the surface. Therefore, it can be concluded that multiple reflection phenomena are highly geometry dependent, and an assumed keyhole shape will certainly lead to incorrect predictions.

D. *Temperature Field*

Figure 4 presents the temperature distribution variation with keyhole depth. Figure 4(1) is the temperature distribution for a flat surface at the reference time. As seen, the temperature at the origin almost reaches the normal boiling point, 3133 K.

As the keyhole deepens, the temperature distribution changes significantly in conjunction with the energy redistribution by multiple reflections. Maximum temperature varies between 3600 and 4000 K, which are 500 to 900 K higher than the normal boiling temperature and ensures an intense evaporation, which, in turn, generates a strong recoil pressure. Comparing the temperature distribution to the laser-intensity distribution patterns (Figure 3), it is obvious that the location of maximum temperature does not necessarily coincide with that of maximum intensity. This can be explained by the time lag originating from the thermal inertia of the material. In fact, the locations for maximum pressure also do not coincide with those of maximum laser intensity, as shown later in Section II.E.

As shown in the figures, the surface temperature far away from the laser-material interaction zone is lower than the inside temperature. This implies that the energy loss by radiation and convection is not negligible. However, this, in part, results from the smoothing of material properties at the L/V interface, which ends up with a much higher thermal conductivity for the gas phase. Thus, there is a possibility that the predicted heat loss at the interface might be overestimated.

E. *Pressure Field*

Figure 5 presents pressure distribution variation with keyhole depth, showing that pressure distribution varies dramatically with the keyhole propagation. Figure 5(1) shows pressure distribution at the reference time. As seen in Figure 5(1), there is no evaporation yet. Therefore, pressure variations in the flow field are small and indistinguishable with the given pressure scale, so the pressure field is shown in almost one color. When evaporation occurs, the entire melt pool is pressurized even though evaporation is a local process.

Maximum pressure at each time-step ranges from 200 kPa (twice the atmospheric pressure) to 600 kPa (six times the atmospheric pressure). Even at places far away from the evaporating surface, the pressure is around 10 to 30 pct higher than the atmospheric pressure. This pressurized melt pool is a characteristic feature of the laser-keyhole welding process and affects subsequent physical phenomena in the weld. The recoil pressure is the key to many characteristic behaviors of the keyhole and neglecting this would result in unrealistic predictions. Many existing models do not incorporate the evaporation phenomena.

F. *Velocity Field*

Figure 6 demonstrates the velocity field variation as the keyhole progresses. As shown, the flow field is very dynamic. Figure 6(1) is the velocity field at the reference time, when there is no evaporation yet. The flow pattern features recirculation zones located at both front and rear parts of the melt pool. Without recoil pressure, it is apparent that the flow field is similar to that in conduction-mode welding.[8,12]

Figure 6(2) shows the flow pattern right after the evaporation starts to occur at the center region. The flow pattern is nearly identical to Figure 6(1), except there is a dominant downward flow starting from the beam center area. As the surface temperature increases well beyond the normal boiling point, the recoil pressure effect becomes predominant, and there is a strong downward flow starting from the evaporation region (Figure 6(3)).

Figure 6(4) shows the flow pattern when the keyhole is relatively shallow. As mentioned earlier, with a shallow keyhole, intensity, temperature, and pressure distributions deviate only a little from the symmetric distribution with a maximum value shifted by a small distance from the coordinate origin. The flow field largely follows the smoothly shaped temperature and pressure gradients.

Figures 6(5) and (6) show the process of the keyhole rear-wall expansion. The flow pattern becomes more complicated due to the growing irregularity and nonconformity in the

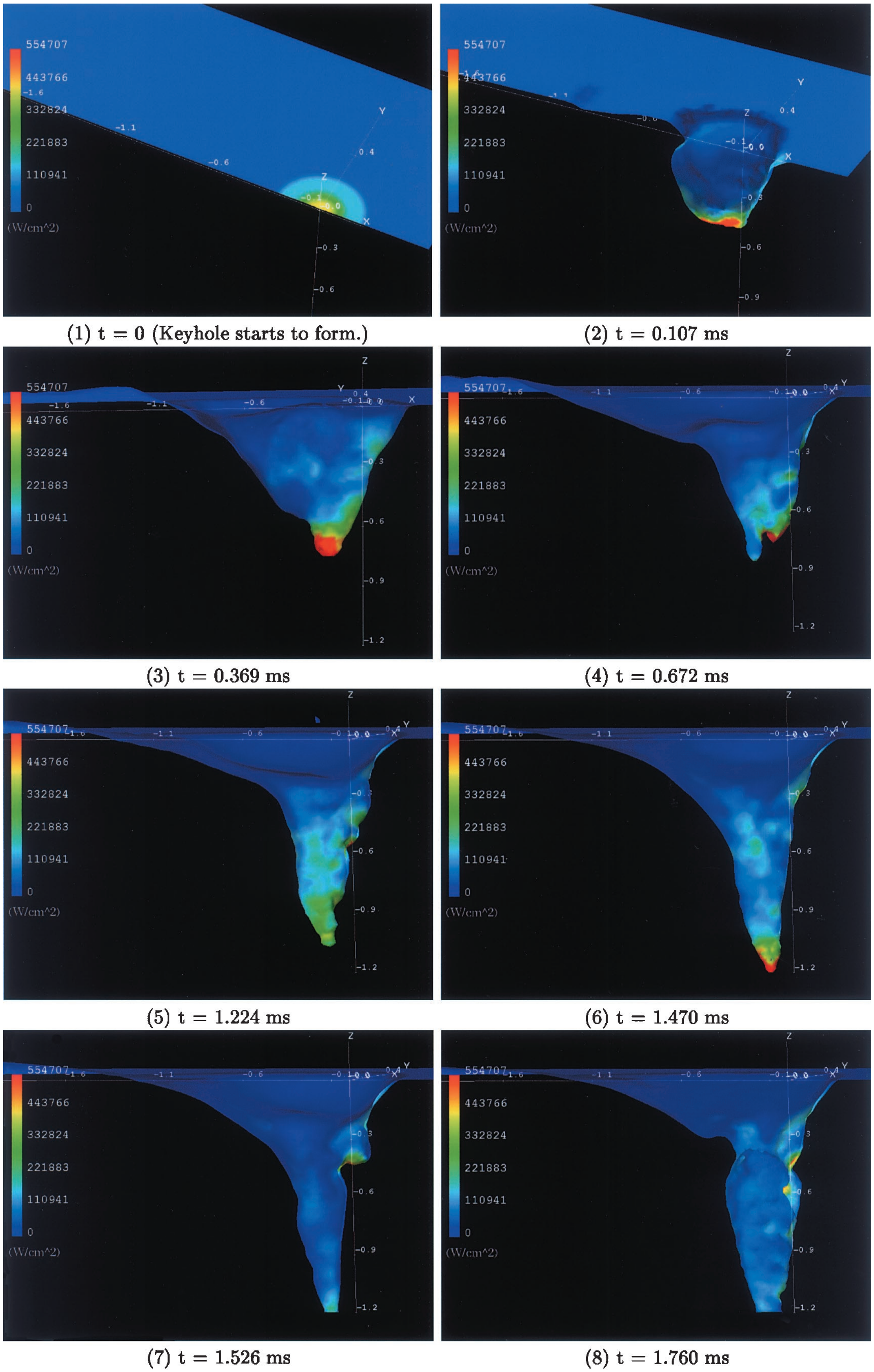

Fig. 3—Laser intensity distribution (laser power: 4 kW, scanning speed: 60 ipm, and beam diameter: 500 μm).

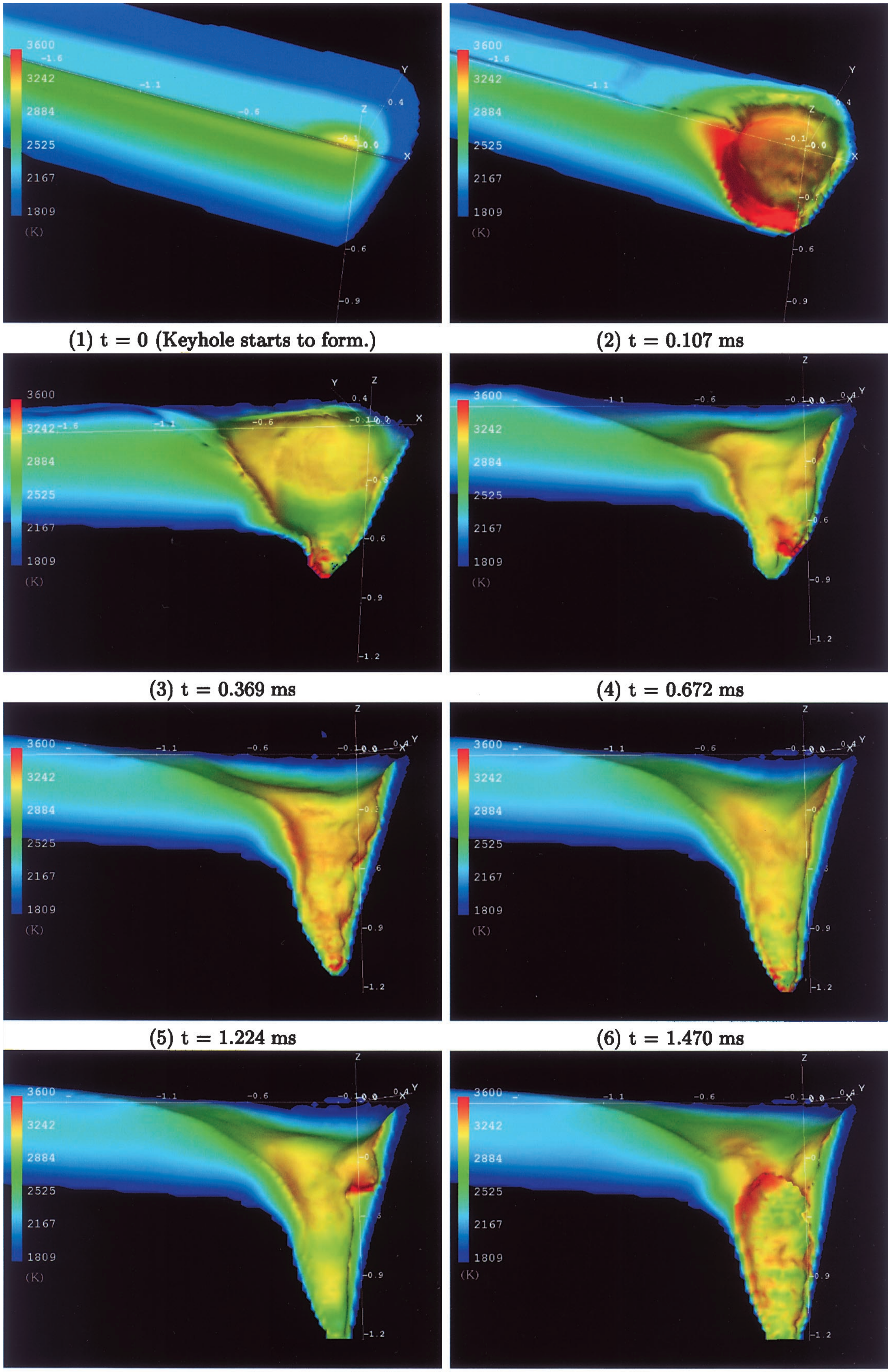

(1) t = 0 (Keyhole starts to form.)

(2) t = 0.107 ms

(3) t = 0.369 ms

(4) t = 0.672 ms

(5) t = 1.224 ms

(6) t = 1.470 ms

(7) t = 1.526 ms

(8) t = 1.760 ms

Fig. 4—Temperature distribution (laser power: 4 kW, scanning speed: 60 ipm, and beam diameter: 500 μm).

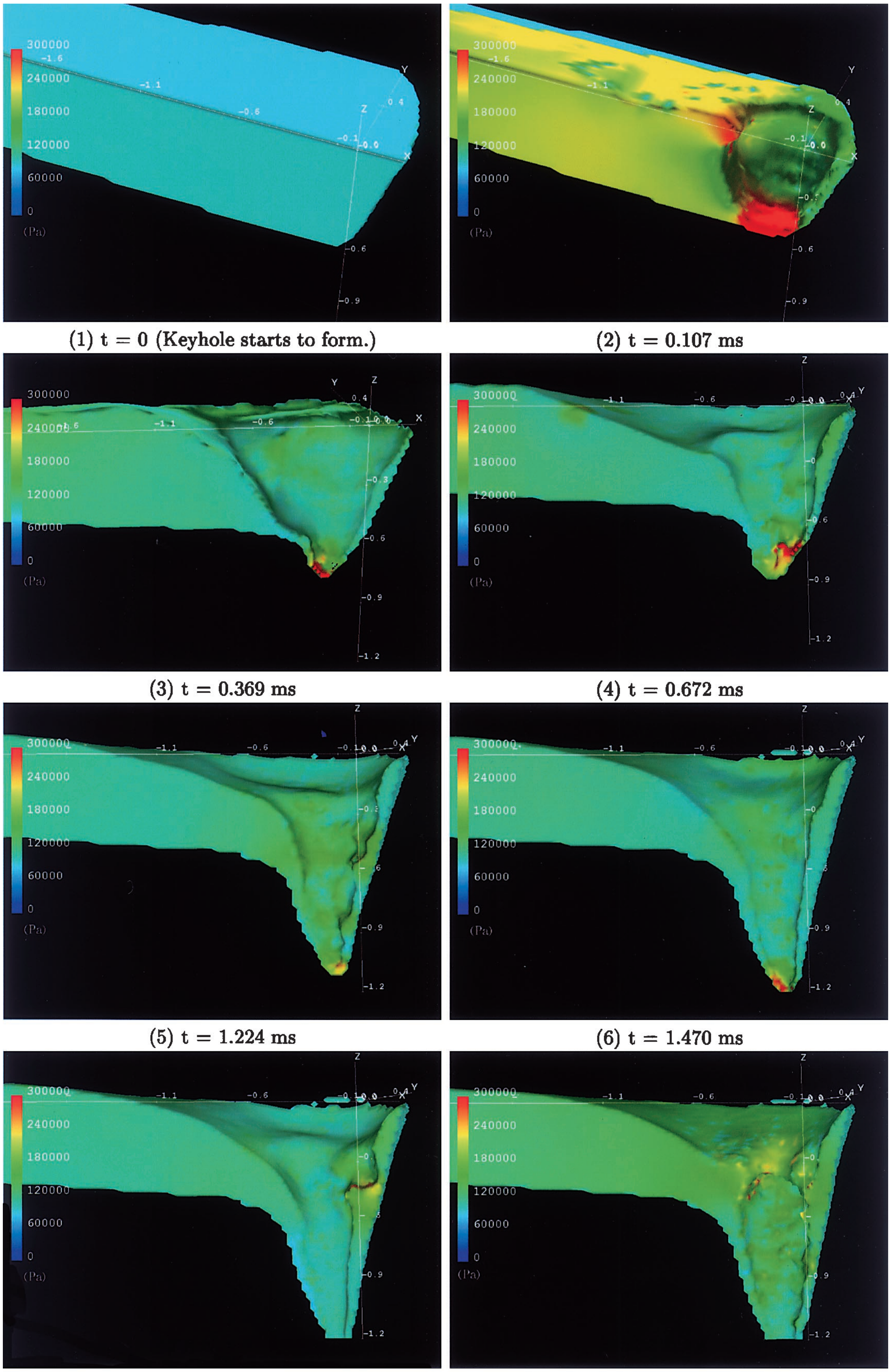

Fig. 5—Pressure distribution (laser power: 4 kW, scanning speed: 60 ipm, and beam diameter: 500 μm).

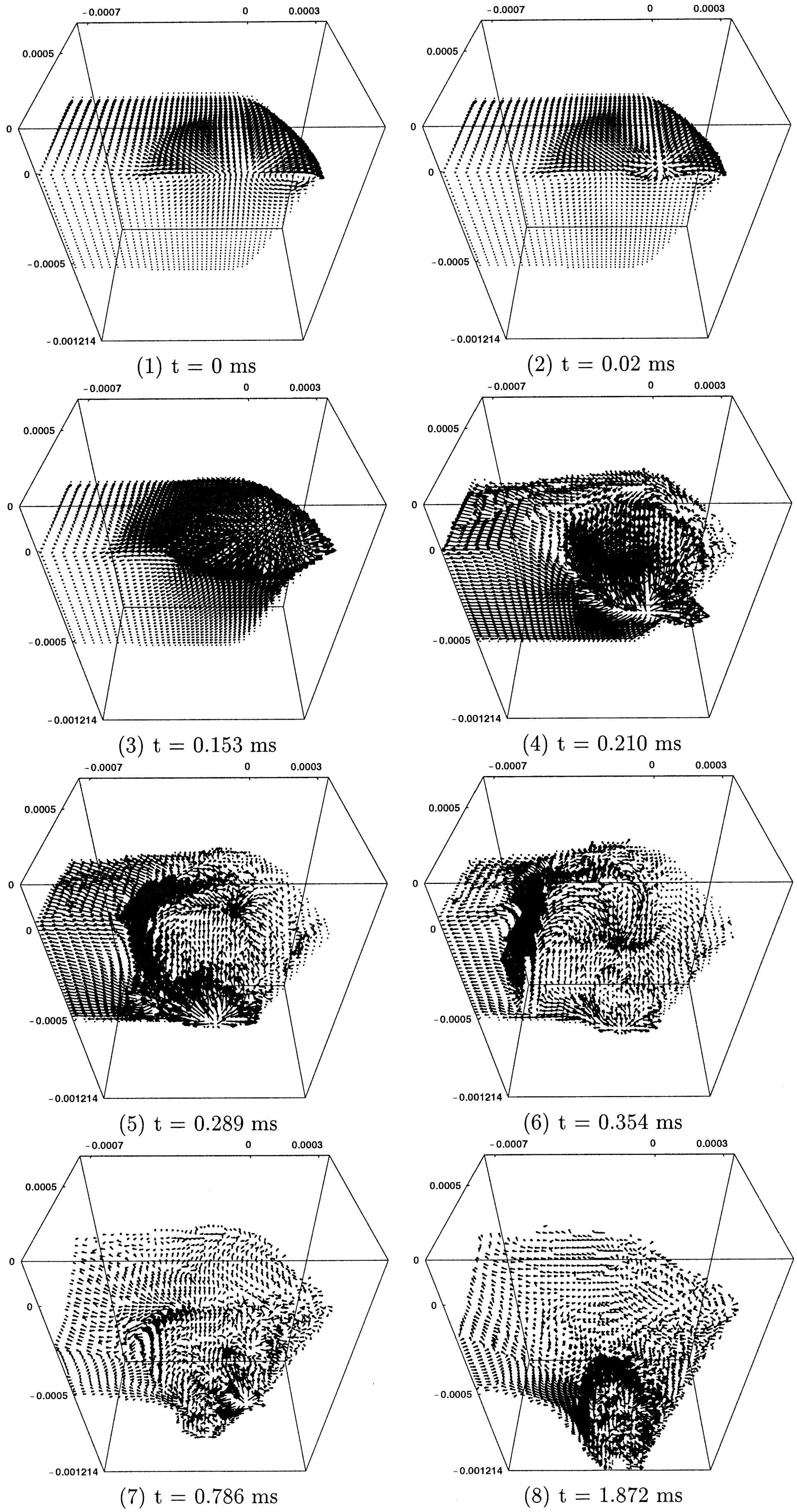

Fig. 6—Velocity distribution (laser power: 4 kW, scanning speed: 60 ipm, and beam diameter: 500 μm).

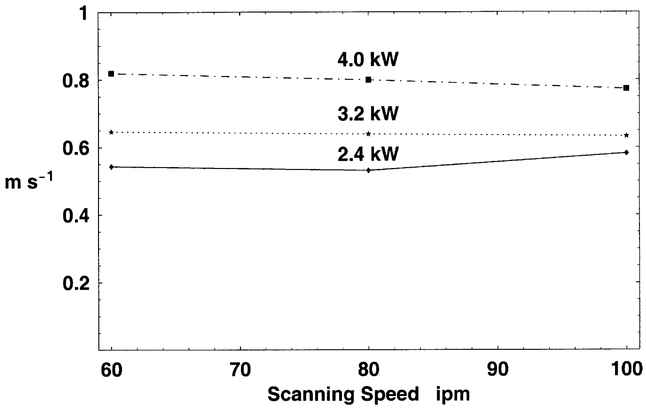

Fig. 7—Average keyholing speed.

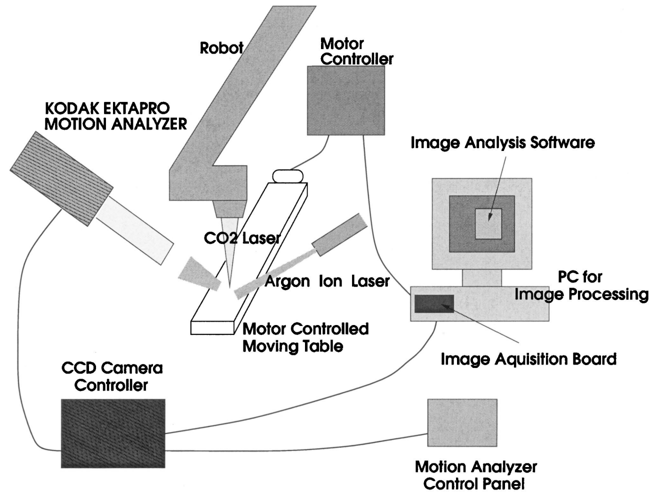

Fig. 8—Schematic of experimental setup.

temperature and pressure fields caused by multiple reflections. As seen in Figure 4(2), the rear wall of the keyhole is strongly heated because the reflected laser beam is concentrating on this region, and consequently, an intensive evaporation occurs at the rear wall. Thus, there is a very strong force that extends the rear wall of the keyhole, and the melt pool can maintain a keyhole that is much larger than the laser-beam diameter.

Figures 6(7) and (8) are the flow fields with a deep keyhole. The flow pattern is very irregular in both cases. In Figure 6(8), we can locate a strong wave going up on the rear keyhole wall. In fact, these types of waves are observed continuously during the entire simulation. The waves are first generated near the coordinate origin located on the front keyhole wall and move down to the bottom of the keyhole and then move up on the rear keyhole wall. By analyzing intensity and temperature field data at each time-step, it has been revealed that these strong waves are created due to the nonuniform localized heating by the laser beam on the front keyhole wall. This localized heating causes formation of humps on the front keyhole wall, which, in turn, accelerates the nonuniform heating of the humps. Thus, a strong melt flow begins due to an excessive increase in recoil pressure. A similar result was presented by Semak and co-workers.[7,9] They predicted the formation of humps on the front keyhole wall with varying welding speed.

G. *Average Keyholing Speed*

Figure 7 is the average keyholing (or drilling) speed calculated for various combinations of laser power and scanning speed. These average speeds are obtained by dividing the target thickness by the penetration time. As expected, it is seen that keyholing speed increases with laser power. And, keyholing speed is inversely proportional to beam scanning speed, except for the $P = 2400$ kW and $V_s = 100$ ipm case, where full penetration could not be achieved and calculating keyholing speed is difficult and inaccurate. For a laser power of 4 kW, the average keyholing speed is about 0.8 m/s.

III. MEASUREMENT OF MELT-POOL GEOMETRY AND FLUID VELOCITY

In this section, the experimental procedure is presented. An optical visualization method[11] is applied to measure the melt-pool geometry during the welding experiment. A new method is proposed for estimating the melt-flow velocity at the surface by measuring the velocity of a hump (or a disturbance), which is convected with a current.[3]

A. *Experimental Setup*

Figure 8 shows the schematic of the experimental setup. A Trumpf (Stuttgart, Germany) 6 kW CO_2 laser system is used as a heat source. To protect oxidation of the target, helium gas is supplied to the melt pool. During the laser welding process, an argon-ion laser beam is used to illuminate the weld-pool surface, and the reflected images are filtered through the narrow-band pass filter. This filter transmits the wavelength of the argon-ion laser (515.5 nm) and is located before the high-speed CCD camera. Images are acquired through the high-performance image-grabbing board and processed by image analysis software to present information on the weld-pool geometry and melt-flow velocity. In this research, VISILOG* 5.0 by Noesis and INSPECTOR** 3.0 by Matrox have been used.

Before performing the experiment, the software must be accurately calibrated so that it can manipulate the images with their real-world dimensions. Besides, rotation and perspective distortions must be removed. To calibrate, a thin paper with a 1×1 mm grid system is attached on the metal coupon, which is identical in thickness to the welding specimen, and the acquired image is calibrated by the software.

A diffuser plate is used to obtain a better resolution of the images.[11] Addition of diffused light makes a tremendous difference in the ability to see the molten surface. In this study, a 1500-grid diffuser plate has been placed right in front of the argon-ion laser.

B. *Measurement of Melt-Flow Velocity at the L/V Interface*

In this section, a method of measuring melt-flow velocity is proposed. Observations reveal that the keyhole fluctuates

*VISILOG is a trademark of Noesis Vision Inc., Paris, France.
**INSPECTOR is a trademark of Matrox Electronic Systems Ltd., Canada.

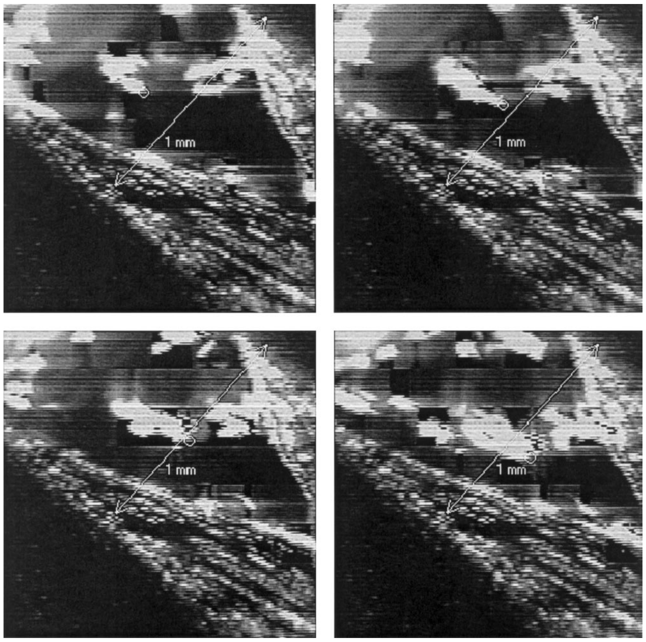

Fig. 9—Illustration of velocity measurement technique: four successive images obtained from the CCD camera capture a wave crest flowing on a current.

rapidly and constantly generates many disturbances over the entire flow field. Those disturbances move toward the weld-pool tail with the main melt flow. The velocity of the disturbance (or a hump) moving on a current at a moderately constant speed, is measured, and this measurement is believed to be reasonably close to the actual flow velocity. Due to the flow unsteadiness caused by the fluctuating keyhole, however, it is difficult to define a velocity at a single point.

The idea is shown in Figure 9. It shows four successive frames where a hump, the tip of which is marked by a small circle, is tracked while being convected toward the tail of the weld pool. The hump velocity can be calculated by measuring the distance between the circles in two successive frames divided by the time elapsed between the frames. Since the melt-flow velocity is large while the time scale of laser welding is very small, a high-speed CCD camera is used at a maximum frame speed of 40,500/sec to obtain flow velocity. As seen in the figure, the small hump is moving on a current, and it propagates due to its own wave nature, as well. In addition, the hump eventually dies out due to viscosity.

This method is similar to the particle tracking velocimetry (PTV). In PTV, some seed particles are used to visualize the flow field, and their motions are tracked instead of the actual flow velocity. By using seed particles, which have similar density to the fluid, one can claim that the measured particle velocity is close to the flow velocity. Likewise, in the method proposed in this study, the surface hump velocity is measured instead of adding any seed particles. Then, the authors claim that the measured velocity is reasonably close to the real melt-flow velocity at the point. In this way, there is no need to compensate for the inertia effect as in PTV, since such humps do not have mass. Meanwhile, they have some degree of wave characteristic and the corresponding

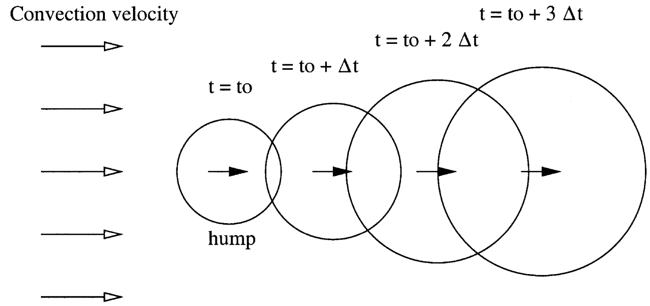

Fig. 10—Illustration of a hump moving on a current. It is convected with the current and propagates outward well. It behaves as a point wave source and becomes bigger as time elapses.

phase velocity. As a result, the hump shows some relative motions with respect to the actual melt flow.

The whole process is illustrated in Figure 10. From the figure, it is obvious that we can minimize the error involved in the relative motion by tracking the center of the hump, which is least affected by the wave characteristic. In other words, the observed velocity of the hump, V_{measured}, can be written as[1]

$$V_{\text{measured}} \approx V_{\text{convec}} + V_{ph} \qquad [1]$$

where V_{convec} is the fluid velocity we want to know, and V_{ph} is the phase velocity of the wave. At the center of the hump, the phase velocity is close to zero, which yields

$$V_{\text{convec}} \approx V_{\text{measured}} \qquad [2]$$

However, it is very difficult to accurately locate the hump center, so the tip of the hump is tracked in this study (Figure 9), which entails some inaccuracy.

If we know a correct equation for V_{ph}, we can obtain a better estimation of the melt-flow velocity. The phase velocity, in general, is obtained from the dispersion relation and is defined as

$$V_{ph} = \frac{\omega}{k} \qquad [3]$$

where ω and k are angular frequency and wave number, respectively. The phase velocity varies tremendously depending on the wave number. The wave number determines whether the surface tension dominates the force of gravity. The type of wave changes from gravity to capillary-gravity to capillary wave as the wave number increases.[1,5] Since wave number is the number of wave crests in a distance of 2π, k is a big number in this problem. It is observed that the length scale of the hump is approximately 0.3 mm. Using this value as the wavelength yields a wave number of 20,944. This wave number corresponds to the capillary wave regime, where the surface tension effect is predominant and phase velocity decreases as wave number increases. However, there are many more factors to take into account in this problem. Deriving an accurate dispersion relation for such complex thermal-fluid problems as laser keyhole welding is extremely challenging and is out of this study's scope.

IV. EXPERIMENTAL MEASUREMENTS *vs* MODEL PREDICTIONS

Due to the loss in the beam delivery system, the maximum available power available in our set up is 4 kW. To compare

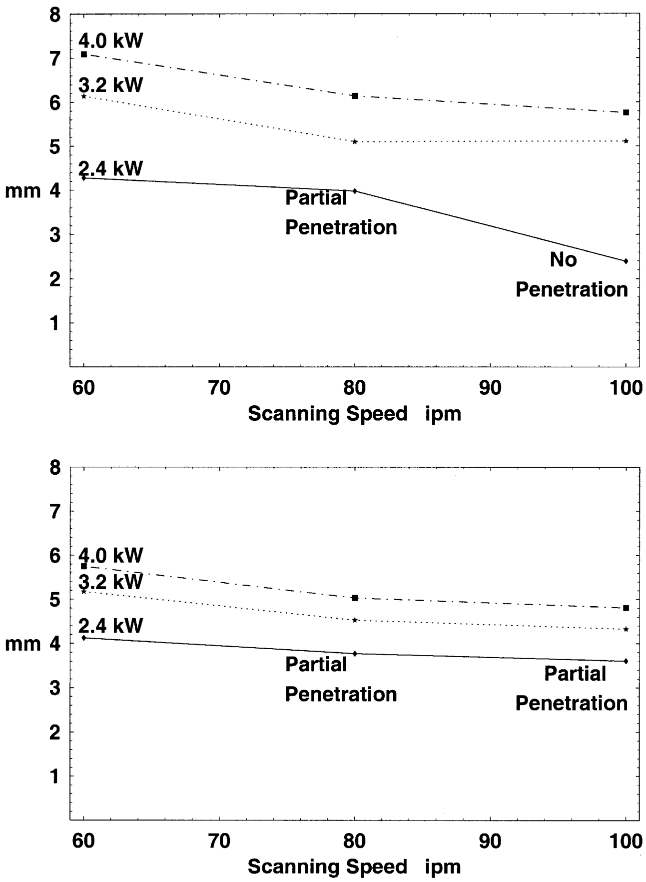

Fig. 11—Laser melt-pool length (mm): top: experimental measurement using the visualization method and bottom: Predictions by simulation.

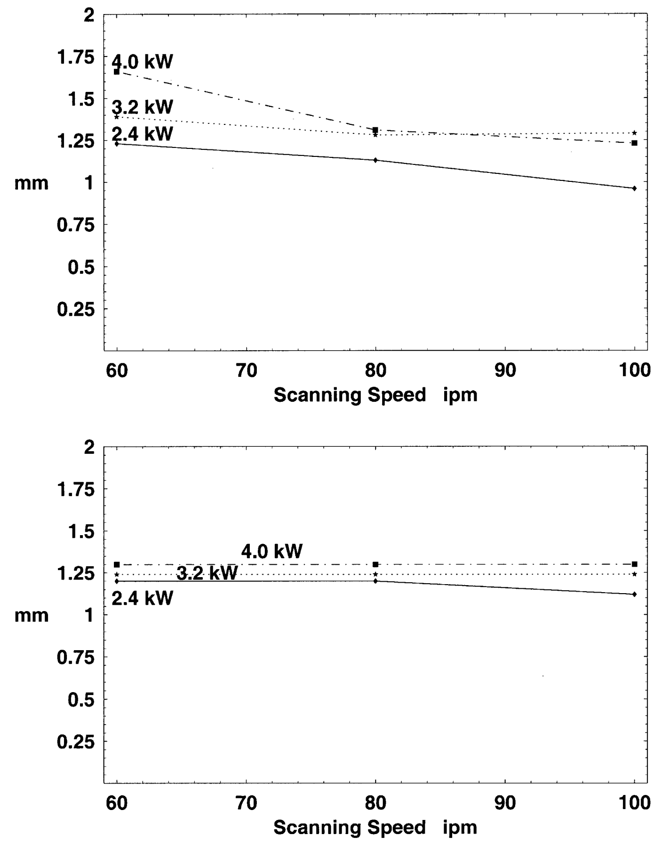

Fig. 12—Laser melt-pool width (mm): top: experimental measurement using the visualization method and bottom: predictions by simulation.

with the simulation result, the same matrices for both laser power (2.4, 3.2, and 4 kW) and scanning speed (60, 80, and 100 ipm) are selected. Mild steel coupons of 1.214-mm thickness, which is also used for a simulation parameter, are chosen as the substrate material. Since the flow field is very unstable, the experiment was repeated ten times and an ensemble average was taken.

Figures 11 through 13 show how the weld pool length, width, and melt-surface velocity change with the laser power and beam scanning speed. Both experimental data and simulation results are shown together.

A. *Melt Pool Geometry*

Figures 11(top) and 12(top) are the experimentally measured, weld-pool length and width. It is obvious that the melt-pool length and width decrease as scanning speed increases and laser power decreases. For relatively high laser powers of 3.2 and 4kW, however, the amount of pool length decrease is small especially when the scanning speed is high (from 80 to 100 ipm). The same is true for the pool width variation. In fact, for the highest scanning speed, the pool width seems to increase as laser power decreases from 4 to 3.2 kW, making the two lines cross. This tendency is even more noticeable in the velocity measurement. It is clearly shown that the length of the weld pool is very long, compared to that of conduction-mode welding. For the highest laser power and the lowest scanning speed, the observed melt-pool length exceeds 7 mm. In conduction-mode welding, the melt-pool length is small (around 1 to 2 mm), even though the same laser power and translation speed are used.[4] To explain how the change of welding mode can affect the size of the melt pool, the keyhole opening time has been observed during the experiment. As marked in Figure 11, we had full penetration for all cases except two. Only partial penetration is observed for the lowest laser power with the intermediate scanning speed. No penetration occurs, and the length of the melt pool decreases to around 2.4 mm for the lowest laser power with the highest scanning speed. This reduction in melt-pool size is ascribed to the disappearance of the keyhole.

Figures 11(bottom) and 12(bottom) are the simulation counterparts of Figures 11(top) and 12(top), respectively. This simulation tends to underestimate the keyhole geometry, and this tendency is more prominent for a higher laser power. In fact, simulation results are very close for lower power cases. For example, measurement and simulation results match within 5 pct for $P = 2400$ kW and $V_s = 60$ ipm, while the computed weld pool length for $P = 4000$ kW and $V_s = 60$ ipm is 75 pct of the measured value. Unlike the experiment, we still have partial penetration for the $P = 2400$ kW and $V_s = 100$ ipm case. Overall, simulation results agree reasonably with the measurement data.

It should be noted that calculating the weld-pool width from the simulation data is not an accurate process due to the small number of grid points in the y direction. In addition,

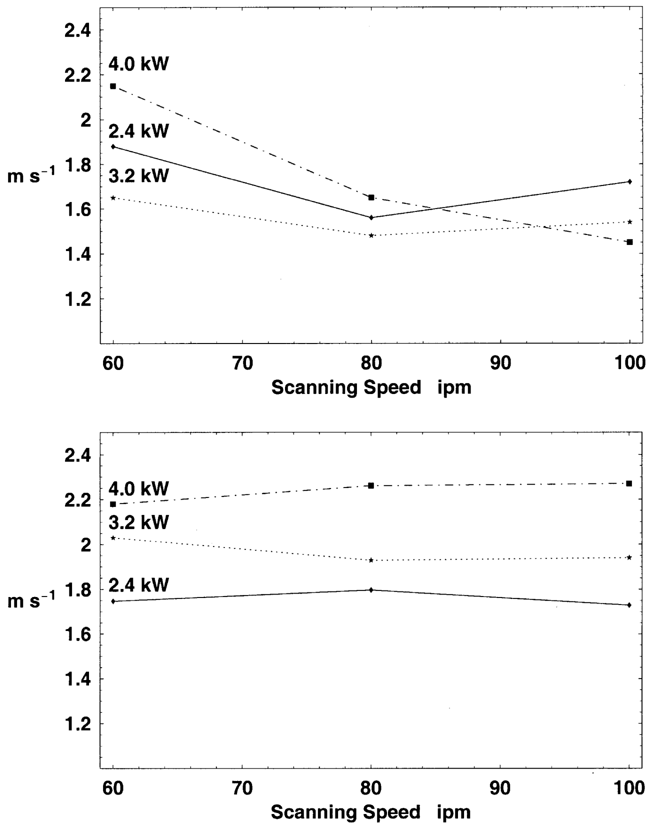

Fig. 13—Melt surface velocity (m/s): top: experimental measurement using the visualization method and bottom: predictions by simulation.

unlike the weld-pool length (*x* direction), the width variation is small.

B. *Melt Surface Velocity*

Figure 13(top) presents the measured melt-surface velocity against the laser power and scanning speed. Since the measurement method provides only one velocity value due to the ensemble averaging, the simulation data must be processed into a single value for comparison. For this reason, the authors attempt to take five node points, which are located 1.2 mm downstream from the coordinate origin, and average the velocity values. Figure 13(bottom) is obtained in this way.

In Figure 13(top), the experimentally obtained velocity values all lie between 1.4 and 2.2 m/s. Overall, velocity increases with laser power and decreases with the scanning speed. However, the plot shows an irregular pattern at high scanning speeds just as in the melt length and width.

As seen in Figure 13(bottom), simulation results range from 1.75 to 2.3 m/s and are reasonably close to the experimental observations. The predicted values are in all cases larger than the measurement data, and the difference is more significant for higher scanning speed. In fact, the simulation results show virtually no dependency on the scanning speed.

Matsunawa[6] observed the liquid flow in the melt pool by preplacing fine tungsten particles of a 100 to 400-μm diameter between the two thin plates and analyzed the trajectories of the W particles. They reported that the W particle moves quickly along the front keyhole wall at 0.4 m/s, and the speed near the eddy reaches 0.25 to 0.35 m/s. In their measurement, there was some uncertainty due to the density difference between the W particle and the target material. The fact that they measured the velocity inside the melt pool below the surface also shows lower velocity as evidence in modeling data presented in Figure 6. In view of the foregoing, the obtained velocity of approximately 1 to 2 m/s from reflective topography is very reasonable. Since the entire flow field is driven by surface phenomena, such as thermocapillary force and recoil pressure, it is believed that there must be a huge velocity gradient at the L/V interface, and therefore, the surface velocity is much higher than that inside the pool.[8]

V. CONCLUSIONS

Simulation and experimental results presented in this article have demonstrated many interesting features of laser-keyhole welding. In summary:

1. The keyhole welding model presented here fully simulates fluid flow and heat transfer in three dimensions, together with the self-consistent keyhole formation. For flow simulations, complete L/V interface boundary conditions, including thermocapillary, capillary, and recoil pressure effects, are used.
2. This study reveals that the evaporation-generated recoil pressure is the major contributing factor that differentiates keyhole-type welding from conduction-type welding.
3. It is demonstrated that any arbitrary surface shape can be simulated by the level set method, without over simplifying the process physics.
4. The effective laser absorptivity keeps fluctuating as a keyhole deepens. Therefore, it is apparent that keyhole fluctuation is an intrinsic phenomenon that originates from the fluctuation in the amount of laser energy absorbed by the keyhole. Keyhole fluctuation and energy absorption pattern are intimately connected. Any fluctuation in the keyhole would affect the energy distribution within the keyhole, which, in turn, affects keyhole fluctuation *via* recoil pressure and flow field around.
5. The laser-intensity profile for laser-keyhole welding shows a very complicated pattern, and the keyhole does not highly concentrate the laser energy on a tiny region.
6. A series of humps were observed to form on the front keyhole wall due to the localized laser-beam concentration by multiple reflections. These humps, in turn, accelerate the nonuniform heating of the humps.
7. The geometry and surface velocity measurements for the laser-keyhole welding process support the validity of the laser welding model proposed.
8. The melt-surface velocity predicted by the simulation is in good agreement with the experimental prediction. Both the welding model and the velocity measurement technique are reasonably accurate. The predictions from this model now can be used to study the microstructure and property evolution in laser-welded joints.

ACKNOWLEDGMENTS

This work was made possible by the continued support of the Office of Naval Research under Grant No: N00014-97-1-0124. Dr. George Yoder is the program manager. The authors also acknowledge the National Center for Supercomputing Applications, or NCSA.

REFERENCES

1. I. Currie: *Fundamental Mechanics of Fluids*, 2nd ed. McGraw-Hill, Singapore, 1993.
2. S. Fujinaga, H. Takenaka, T. Narikiyo, S. Katayama, and A. Matsunawa: *J. Phys. D: Appl. Phys.*, 2000, vol. 33, pp. 492-97.
3. H. Ki, P. Mohanty, and J. Mazumder: filed for U.S. Patent, 2001.
4. H. Ki, P.S. Mohanty, and J. Mazumder: *Metall. Mater. Trans. A*, 2002, vol. 33A, pp. 1817-30.
5. L. Landau and E. Lifshitz: *Fluid Mechanics*, 2nd ed., Pergamon Press, Singapore, 1989.
6. A. Matsunawa: *Keyhole Dynamics in Laser Welding*, Technical Report, Lecture Note from a Course Given at ICALEO, San Diego, CA, 1999.
7. A. Matsunswa and V. Semak: *J. Phys. D: Appl. Phys.*, 1997, vol. 30, pp. 798-809.
8. J. Mazumder: *Opt. Eng.*, 1991, vol. 30 (8), pp. 1208-19.
9. V.V. Semak, W.D. Bragg, B. Damkroger, and S. Kempka: *J. Phys. D: Appl. Phys.*, 1999, vol. 32, pp. L61-L64.
10. W.M. Steen: *Laser Material Processing*, 2nd ed., Springer, London, 1998.
11. D.D. Voelkel and J. Mazumder: U.S. Patent 5,446,549, Aug. 1995.
12. R.L. Zehr: Ph.D. Thesis, University of Illinois at Urbana-Champaign, Urbana, IL, 1991.